Analytical bond model for general type of reinforcements of finite embedment length in cracked cement based materials

C. A. Nonato Da Silva[a], J. Ciambella[a,*], J. A. O. Barros[b], I. G. Costa[c]

[a] *Department of Structural and Geotechnical Engineering, Sapienza University of Rome, Italy*
[b] *Departamento de Engenharia Civil, University of Minho, Portugal*
[c] *Civitest - Pesquisa de Novos Materiais para a Engenharia Civil, Portugal*

Abstract

In this work, a computational model for simulating the relevant mechanisms governing the pull-out of a discrete reinforcement embedded into cement based materials is described. The model accounts for the material and geometric properties of the reinforcement, which can include an anchored end, the interface between reinforcement and surrounding medium, and the relative inclination of the reinforcement to the crack plane. The reinforcement is modelled as a Timoshenko beam resting on a cohesive-like foundation that allows all the failure modes seen in the experiments to be accounted for, namely: debonding at the interface between the reinforcement and the concrete, cracking and spalling of the concrete matrix, rupture of the reinforcement. A comprehensive comparison with the experimental data available in the literature highlights the good predicting capabilities of the proposed model in terms of both peak force and dissipated energy. Furthermore, since the model is capable of simulating a discrete reinforcement of any direction towards the crack plane, complex mechanisms like micro-spalling of the matrix at the exit point of the reinforcement can be captured conveniently. By carrying out parametric analysis is possible to optimize the geometry of the anchored ends for maximizing the peak force and/or the energy dissipation in the pull-out process. Therefore, the developed model

*Corresponding author

constitutes a relevant numerical tool for the optimization of discrete and continuous reinforcements of concrete structures including Fibre Reinforced Polymer (FRP) systems and Steel Fibre Reinforced Concrete (SFRC).

Keywords: Reinforcement mechanisms, FRP, SFRC, Timoshenko beam, Cohesive interface

---

1. Introduction

Concrete is characterized by a low tensile strength that requires the use of proper strengthening mechanisms in case of tension-dominant loadings. In the last decades, Fibre Reinforced Polymer (FRP) systems have been used to ensure the aimed flexural and/or the shear capacity of new concrete structures or in the context of structural rehabilitation, due to the recognized favourable benefits of these composite materials (Bakis et al., 2002). Short fibres (predominantly steel fibres) have been also used to increase the post-cracking tensile capacity of cement based materials, as a partial, or even total, replacement of conventional steel reinforcements for shear capacity of RC beams (Meda et al., 2005; Barros and Foster, 2018), flexural capacity of slabs on soil (Barros and Figueiras, 1998), slabs supported on RC columns (Barros et al., 2017), for strengthening of RC columns (Ganesan and Murthy, 1990), and even in tunnelling (Tiberti et al., 2014). By offering resistance to crack opening, discrete fibres are also very effective in improving the durability of concrete structures (Brandt, 2008). These benefits are, however, only significant when debonding is the governing failure fibre mechanism, which requires a good balance between fibre geometry including anchorage conditions, fibre material properties (tensile strength and elasticity modulus), and stiffness and strength of the surrounding cement matrix (Naaman and Najm, 1991; Bentur and Mindess, 2007). In the technology of Fibre Reinforced Concrete (FRC), the most effective anchorage conditions are being assured by steel fibres, due to technological aspects of fibre production and steel stiffness, and the resulting cement based composite material is designated by Steel Fibre Reinforced Concrete (SFRC), which is still the most used in structural applications.

For reliable modelling of the reinforcement mechanisms of discrete fibres in the FRC technology, as well as in FRP systems, is essential to comprehend the pull-out behaviour of a single reinforcement. With this intent, extensive experimental researches were carried out with steel fibres in cementitious matrices (Cunha et al., 2009; Fantilli and Vallini, 2007; Isla et al., 2015; Laranjeira et al., 2010; Leung and Shapiro, 1999; Mazaheripour et al., 2016; Robins et al., 2002; Zhan and Meschke, 2014; Zīle and Zīle, 2013) as well as with concrete reinforced with FRP (Bilotta et al., 2016; Caggiano et al., 2012; Cosenza et al., 1997; Sena-Cruz and Barros, 2004; De Lorenzis et al., 2002; Echeverria and Perera, 2013; Focacci et al., 2000; Seracino et al., 2007). The results from the experimental programs in these domains are being used for deriving constitutive laws that simulate the bond behaviour between these reinforcements and surrounding cement-based matrix. In this context, Cunha et al. (2009) developed a numerical strategy to calibrate the parameters of the local bond stress slip relationship for smooth and hooked ends steel fibres of different orientation regarding the loading direction (from 0 to 60 degrees). By considering a spring at the extremity of the smooth central part of the fibre, the anchorage mechanism provided by the hooked end was simulated. Laranjeira et al. (2010) developed an analytical model based on the key states of the pull-out process; at each stage, the load magnitude and the crack width were predicted by using a multi-linear slip-bond stress interface law. Li et al. (1990) simulated the fibre pull-out as a beam element supported on an elastic medium. In their model, the fibres were so flexible that all deformations were assumed to occur around the exit point of the fibre and, therefore, the fibre was idealized as a string passing through a frictional pulley. Fantilli and Vallini (2007) presented a formulation for inclined steel fibre modelled as a beam on elastic foundation with friction coefficient between the materials and a Mohr-Coulomb failure criterion for the matrix. Despite good agreement with experimental results, the spalling of the matrix and the fibre bending that were widely observed in the experiments (Lee and Foster, 2006, 2007), were mostly disregarded in the modelling.

Concerning FRP systems, Sena-Cruz and Barros (2004) carried out experiments to calibrate the parameters that define the local bond relationship for aligned Carbon Fibre Reinforced Polymer (CFRP) strips. In Focacci et al. (2000), the authors presented a method to determine the slip-bond stress relationship from the results of pull-out tests that take into account the distribution of slip and bond shear stress along the embedded portion of the reinforcement. However, they found consistent results only for high values of reinforcement embedment lengths. An analytical formulation based on the Malvar model was used in Cosenza et al. (1997) to represent the bond-slip behaviour. The model closely matched the pull-out behaviour in the ascending branch of the force-displacement curve, but failed to describe the descending branch. An analytical formulation of the global behaviour of FRP plates bonded on an external support was presented in Caggiano et al. (2012) and was used to investigate the behaviour of composite plates externally bonded to other materials such as steel, wood or masonry, but its applicability is restricted to the Externally Bonded Reinforcement (EBR) technique.

All these contributions show that the mechanisms governing the pull-out response of reinforcement systems forming a certain inclination with the loading direction are significantly different from those activated for an aligned reinforcement. Besides debonding and friction along the reinforcement-matrix interface, additional mechanisms such as reinforcement bending and matrix spalling at reinforcement exit point generally occur. Furthermore, the contributions of these micromechanisms depend on the reinforcement inclination angle, the embedment length and the matrix properties that have to be considered in the modelling process. In the experiments carried out by Cunha et al. (2009) the peak pull-out force of an inclined fibre was observed to be higher than an aligned one, as long as the fibre does not fail in tension and micro-spalling of the concrete does not occur. In fact, above a certain inclination of the fibre, which was around 45° (a value that depends on the fibre tensile strength and stiffness, as well as on the matrix strength), the peak pull-out force has tended to decrease with the increase of the fibre inclination. **The experimental results**

presented by Leung and Shapiro (1999) reveal that the fibre tensile strength clearly has an effect on the crack bridging efficiency of inclined steel fibres, which represent most of the fibres in the quasi-random distribution found in practical cement composite systems. Several investigations reported similar tendencies and have concluded the existence of an optimal configuration for which the load and the energy absorption capacity are maximal (Cunha et al., 2009; Laranjeira et al., 2010; Zhan and Meschke, 2014).

In this paper, a novel analytical model incorporating the key morphological feature of reinforcement-matrix microstructure is developed. The model simultaneously accounts for all the relevant effects seen in the pull-out response which are mostly neglected in the available literature contributions, namely: (i) the bending of the inclined fibre, (ii) the damage of the concrete matrix at the fibre exit point, and (iii) the change on the embedment length due to matrix spalling. The reinforcement is modelled as a Timoshenko beam resting on a nonlinear elastic foundation and the differential equations that govern the pull-out behaviour are solved, by considering the variation of the axial and transversal displacements, the axial and shear forces, and the bending moment along the reinforcement length. As such, the model is able to account for all the failure mechanisms observed in the experiments, including reinforcement debonding and rupture, and matrix spalling.

By performing numerical simulations with a commercial finite element software, the model is validated and a good predictive performance is demonstrated. The model capabilities are also assessed by simulating available experimental fibre pull-out tests. The parameters that define the interface and foundation were obtained from the experimental results in Cunha et al. (2009) and Leung and Shapiro (1999). Finally, by conducting a parametric analysis, it is shown that there are optimal geometries for the fibre anchorage mechanisms that maximise the fibre peak pull-out force and the energy dissipation.

The structure of the paper is as follows. In Sec. 2 the analytical formulation of the model is described, Sec. 3 details the model implementation and its validation with a commercial FE code. In Sec. 4 the predicting capabilities of the model are assessed by simulating the fibre pull-out tests carried out by Cunha et al. (2009) and Leung and Shapiro (1999), showing a good agreement with the experiments. A sensitivity analysis is carried out in Sec. 5 to identify the optimal configuration of the fibre anchored ends. The main conclusions of this study are presented in Sec. 6.

2. Model formulation

The model aims to predict the pull-out behaviour of a reinforcement constituted by two segments, one aligned with the loading and another forming an angle (θ) with the previous one (Figure 1a). This type of reinforcement configuration was used by Barros et al. (2017) for the simultaneous flexural and punching strengthening of RC slabs using an innovative CFRP laminate, but can also be used to simulate steel fibre with an inclination towards the crack plane, under the framework of SFRC. If the load vs displacement response could be accurately captured, this model can then be extended to simulate more complex anchorage conditions, such are those ensured by discrete hooked end steel fibres. Furthermore, the present approach focus on the use of a relatively small number of physical parameters, which allows a robust optimisation strategy to be pursued.

2.1. Geometry

The proposed model is defined by seven geometric parameters, some of which are shown in Fig. 1a): the horizontal L_h and inclined L_i lengths of the reinforcement, the inclination angle θ, the cross section areas of the reinforcement in the horizontal A_h and inclined A_i parts, the perimeter of the reinforcement p_h and p_i. Throughout this document, the subscripts h and i are used to indicate the horizontal and inclined parts of the reinforcement, respectively. The proposed

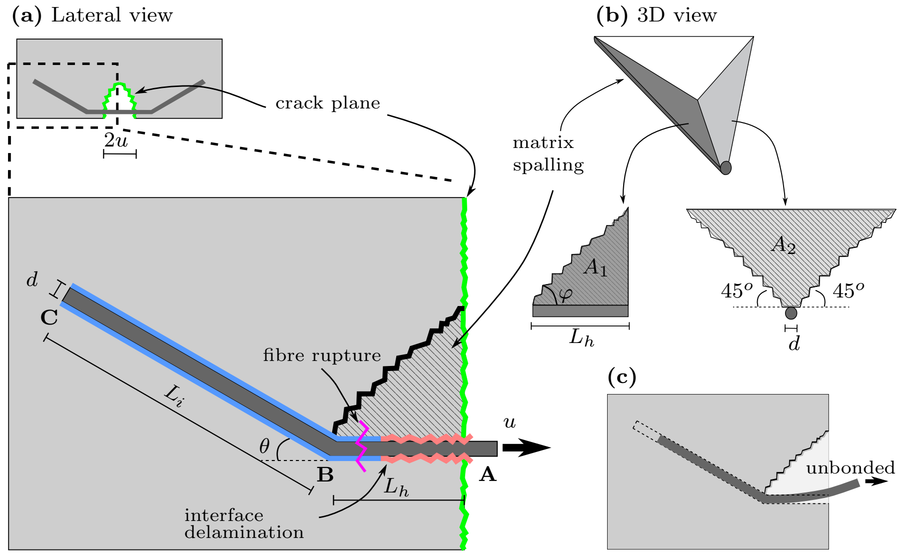

Figure 1: (a) Main geometric parameters of the model with the three possible failure mechanisms highlighted: (i) interface delamination, (ii) matrix spalling and (iii) fibre rupture. The dashed area indicates the region where matrix spalling is likely to occur. (b) and (c) shows respectively the geometry of the matrix wedge and the deformed shape of the fibre once spalling has occurred.

model is intended for reinforcements of the same material in both parts, but can be easily extended to FRP systems with different elasticity moduli in order to describe the type of reinforcement used in Barros et al. (2017). In the following, the material comprising the reinforcement in the horizontal and inclined part was assumed to be the same, thus no distinction is made for the elastic modulus (E) of the two parts.

2.2. Equilibrium equations

By neglecting the thickness of the interface, the force equilibrium along the reinforcement in the axial direction at the **curvilinear abscissa x along the reinforcement** is given by:

$$N'_\alpha(x) = p_\alpha \tau(s_\alpha(x)), \tag{1}$$

where $\alpha = \{h, i\}$, s_α is the sliding of the interface, i.e., the difference between the axial displacement of the fibre and the one of surrounding concrete, τ is the local bond stress on the contact surface between the reinforcement and the concrete and N_α is the axial force in the reinforcement, i.e., axial stress multiplied by the cross-section area $N_\alpha = \sigma_\alpha A_\alpha$. By neglecting the concrete deformability as in (Sena-Cruz and Barros, 2004; Cunha et al., 2009; Kalupahana, 2009), the sliding at the interface can be directly related to the displacement in the reinforcement, i.e., $s \equiv u$, thus the axial equilibrium gives $\tau(u_\alpha(x)) = \frac{A_\alpha}{p_\alpha}\sigma'_\alpha(x)$. Here and henceforth, a prime will indicate the derivative with respect to x. Assuming a linear elastic behaviour for the reinforcement ($\sigma_\alpha = E\epsilon_\alpha$) and being $\epsilon_\alpha = u'_\alpha$, Eq. (1) leads to:

$$u''_\alpha(x) = \frac{p_\alpha}{A_\alpha E}\tau(u_\alpha(x)). \tag{2}$$

The relationship between the stress τ at the interface and the axial displacement is in general, nonlinear. In particular, as demonstrated in the next subsection a cohesive-like interface law will be herein adopted.

In the transverse direction, the reinforcement-matrix system can be idealized as a beam resting on a cohesive-type foundation. The simplest foundation model is the one introduced by Winkler, in which the reaction forces of the foundation are linearly proportional to the deflection of the beam. This model was successfully applied to a number of systems in which the reinforcement had at least one order of magnitude higher stiffness than the matrix (Wang et al., 2005). In this respect, metallic fibres have a Young's modulus of about 200 GPa compared to 20-40 GPa of the surrounding matrix, which justifies the application of the Winker foundation model to this system. However, due to the material nonlinear behaviour observed in experimental tests (Lee and Foster, 2007), a nonlinear foundation model will be adopted and presented in more details in the next subsection.

In addition, to make the model suitable to describe general type of reinforcements, as discrete steel fibres, a Timoshenko beam type model is chosen for simulating the behaviour of the reinforcement. In fact, the hooked ends fibres available in the market have a total length (L_f) that varies between 30 and 60 mm. **For the fibres of minimum length the diameter ranges between 0.2 and 0.4 mm, while for the fibres of maximum length their diameter varies between 0.6 and 1.0 mm. For the shorter fibres the L_i ranges between 2 and 4 mm, while for the longer fibres, L_i varies between 4 and 6 mm. Taking these values into consideration and the fact that the embedment length ($L_b = L_i + L_h$) in SFRC can be statistically considered equal to $L_f/4$ (Wang, 1989), the ratio d/L_i varies between 0.05 and 0.25, thus the shear deformability of the fibre plays a significant role.**

By using the Timoshenko model, the dimensionless transverse displacement v_α and the rotation ϑ_α along the fibre axis x are calculated by solving the differential equations governing the transverse equilibrium at each segment of the beam:

$$T'_\alpha(x) - q(v_\alpha(x)) = 0, \qquad M'_\alpha(x) - T_\alpha(x) = 0\,, \tag{3}$$

where T_α is the shear force, M_α the bending moment at segment $\alpha = \{i, h\}$, q is the reaction force of the foundation (representing the cement based matrix medium surrounding the fibre embedment length), that depends on the transverse displacement. By taking into account the shear deformability of the reinforcement and by assuming that its response is linear, one has $M_\alpha = -EI_\alpha \vartheta'_\alpha$ and $T_\alpha = K_\alpha(\vartheta_\alpha - v'_\alpha)$, which upon substitution in Eq. (3) gives

$$\begin{cases} EI_\alpha \vartheta''_\alpha(x) - K_\alpha \vartheta_\alpha(x) + K_\alpha v'_\alpha(x) = 0 \\ K_\alpha v''_\alpha(x) + q(v_\alpha(x)) - K_\alpha \vartheta'_\alpha(x) = 0 \end{cases} \tag{4}$$

where I_α is second moment of area of the cross section and $K_\alpha = \kappa A_\alpha G$, in which G is the shear modulus of the reinforcement and κ the so-called Timoshenko shear coefficient. In order to have a better understating of the interplaying between the parameters and prepare the model for the numerical implementations, the governing equations in the axial and transversal directions (Eqs. (2)

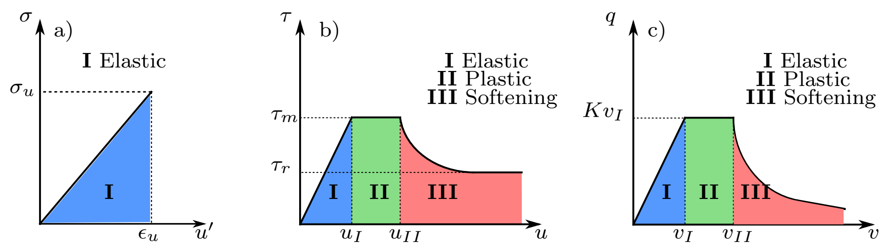

Figure 2: Material models for fibre (a), interface (b) and concrete (c). The coloured areas indicate the three stages of the pull-out process, i.e., elastic, plastic, softening.

and (4)) are now established in dimensionless form through the following non-dimensional quantities:

$$\xi_\alpha = \frac{x}{L_\alpha}, \qquad \hat{u}_\alpha(\xi_\alpha) = \frac{u_\alpha(x)}{L_\alpha}, \qquad \hat{v}_\alpha(\xi_\alpha) = \frac{v_\alpha(x)}{L_\alpha}, \qquad \hat{\vartheta}_\alpha(\xi_\alpha) = \vartheta_\alpha(x), \quad (5)$$

where $\xi_\alpha \in [0, 1]$ is the dimensionless abscissa and a hat $\hat{\cdot}$ is used to indicate the dimensionless form of the variables. Substituting Eq. (5) into Eqs. (2) and (4) leads to the following system of nonlinear ordinary differential equations:

$$\begin{cases} \hat{u}''_\alpha = \chi_\alpha \hat{\tau}(\hat{u}_\alpha), \\ \hat{\vartheta}''_\alpha - \psi_\alpha(\hat{\vartheta}_\alpha - \hat{v}'_\alpha) = 0, \\ \hat{v}''_\alpha + \beta_\alpha\, \hat{q}(\hat{v}_\alpha) - \hat{\vartheta}'_\alpha = 0 \end{cases} \tag{6}$$

where $\alpha = \{h, i\}$, $\chi_\alpha = p_\alpha L_\alpha / A_\alpha$, $\beta_\alpha = EL_\alpha^2 / K_\alpha$, $\psi_\alpha = K_\alpha L_\alpha^2/(EI_\alpha)$, $\hat{q} = q/(EL_\alpha)$ and $\hat{\tau} = \tau/E$ are the dimensionless parameters related to the geometry and material properties of the model. It is noted that in Eq. (6) a prime $'$ indicates the derivative with respect to the dimensionless abscissa ξ_α.

2.3. Material and interface models

To solve the differential equations governing the reinforcement pull-out behaviour, the constitutive laws $\tau(u)$ and $q(v)$ must be specified in Eqs. (2)-(4) (in Eqs. (6)). The reinforcement was considered as having an elastic-brittle behaviour, being the maximum tensile strength equal to σ_u with its corresponding strain ϵ_u (Fig. 2a), whereas for the concrete and the interface a cohesive-like behaviour characterised by three phases was assumed (Figs. 2b and 2c). During the initial stage of the reinforcement pull-out, the matrix and the reinforcement are firmly connected and the interface has an elastic response (elastic stage in Fig. 2b); at a certain level of displacement, assumed defined by u_I, the level of damage at the interface between reinforcement and surrounding matrix is so significant that the interface attains its bond strength, τ_m, resulting in a yield-like behaviour (plastic stage in Fig. 2b); when the cumulative damage reaches a level that converts the cohesive nature of the bond into a frictional type, the bond stress decreases with the increase of the displacement, with a softening-like behaviour (softening phase in Fig. 2b). A horizontal asymptote in the bond stress-displacement diagram is used to account for the residual frictional mechanism between the fibre and the matrix, simulated by the residual bond stress, τ_r.

The three stages of the diagram represented in Fig. 2c aims to simulate the support conditions provided by the concrete medium assuming the following three distinct level of damage in this medium: an elastic phase while the stress level transferred by the reinforcement to the concrete medium do not introduce significant damage; a plastic stage due to the occurrence of plastic deformation and micro-cracking in the concrete; a softening stage due to the degeneration of micro-cracking into a macro-cracking and concrete spalling at the exit point of the reinforcement.

Accordingly, the following cohesive-like interface laws are assumed for $\tau(u_\alpha)$:

$$\tau(u_\alpha) = \begin{cases} \tau_m \dfrac{u_\alpha}{u_I} & if\ u_\alpha \leq u_I \\ \tau_m & if\ u_I < u_\alpha \leq u_{II} \\ \tau_r + (\tau_m - \tau_r)\dfrac{u_{II}}{u_\alpha} & if\ u_\alpha > u_{II} \end{cases} \tag{7}$$

and for $q(v_\alpha)$:

$$q(v_\alpha) = \begin{cases} Kv_\alpha & if\ v_\alpha \leq v_I \\ Kv_I & if\ v_I < v_\alpha \leq v_{II} \\ Kv_I \dfrac{v_{II}}{v_\alpha} & if\ v_\alpha > v_{II} \end{cases} \tag{8}$$

In Eqs. (7) and (8), $\tau_m A_\alpha / u_I$ and $K A_\alpha / v_I$ are the elastic stiffnesses of the interface and the foundation, whereas u_I and v_I represents the maximum displacements when the bond and concrete strength are attained, respectively. These values, in turn, influence the maximum force achieved in the overall force-displacement diagram. The details of the derivation of the constitutive parameters from the experimental data are given in Sec. 4.

2.4. Boundary Conditions

The governing equations in the axial and transversal direction Eqs. (6) for the horizontal and inclined parts can now be solved by the adopted constitutive laws for the interface and concrete support medium (Eqs. (7) and (8)). The pull-out problem is governed by a set of four second-order ordinary differential equations for the transverse displacements and rotations (Eqs. (6.1) and (6.2) for $\alpha = i$ and $\alpha = h$) and two second-order ordinary differential equations for the horizontal displacements (Eq. (6.3) for $\alpha = i$ and $\alpha = h$). Thus, twelve boundary conditions must be specified. The local reference systems used to derive the differential equations as well as the continuity conditions at the intersection of the horizontal and inclined segments are specified in Fig. 3.

At the loaded end of the fibre, (Point A in Fig. 3a), the following conditions are applied:

$$u_h(L_h) = \bar{u}, \qquad v_h(L_h) = 0, \qquad \vartheta_h(L_h) = 0, \tag{9}$$

where $\bar{u}$ is the applied displacement, normally designated as loaded end slip (displacement in the present case since negligible deformation for the concrete at reinforcement exit point was assumed) in the reinforcement pull-out tests. In cracked cement based materials, the displacement/slip ($\bar{u}$) can be considered equal to half of the crack width (see Fig. 1a) (Chasioti, 2017). In order to

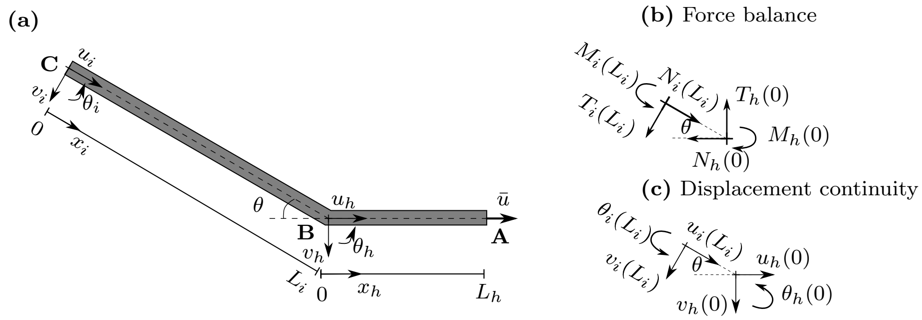

Figure 3: (a) Local reference systems for the two segments of the reinforcement. (b) force balance and (c) displacement continuity at the intersection point B between the horizontal and inclined segments.

reproduce the pull-out test carried out by Cunha et al. (2009), the present model assumes a null vertical displacement in the loaded end. However, different mechanisms at the exit point of the fibre can be simulated by changing these boundary conditions. Concerning the free end (Point C in Fig. 3a), the following boundary conditions are assumed:

$$N_i(0) = 0, \qquad T_i(0) = 0, \qquad M_i(0) = 0. \tag{10}$$

Finally, at the connection between the horizontal and inclined segments (Point B in Fig. 3a), the continuity of forces/moment yields the following conditions (Fig. 3b):

$$\begin{aligned} N_h(0) &= N_i(L_i)\cos(\theta) - T_i(L_i)\sin(\theta), \\ T_h(0) &= N_i(L_i)\sin(\theta) + T_i(L_i)\cos(\theta), \\ M_h(0) &= M_i(L_i), \end{aligned} \tag{11}$$

together with the continuity of displacements/rotations (Fig. 3c):

$$\begin{aligned} u_h(0) &= u_i(L_i)\cos(\theta) - v_i(L_i)\sin(\theta), \\ v_h(0) &= u_i(L_i)\sin(\theta) + v_i(L_i)\cos(\theta), \\ \vartheta_h(0) &= \vartheta_i(L_i). \end{aligned} \tag{12}$$

2.5. Failure criterion for brittle reinforcements

In the pull-out test of a discrete reinforcement, either debonding or reinforcement rupture is observed. These mechanisms can occur with concrete spalling usually starting at the transition between the horizontal and inclined parts (after concrete spalling, the reinforcement embedment length is reduced (Ng et al., 2014)). The reinforcement rupture usually occurs when high strength matrix and/or low tensile strength fibre are used, or if the embedment length is higher than a certain value known as *critical embedment length*, that depends on the inclination of the reinforcement towards the loading direction in the crack plane, the effectiveness of the anchorage mechanisms in the embedment length, and the material tensile rupture (Barros and Foster, 2018). The reinforcement rupture condition in any section is due to the combined effect of bending moment M_α, axial N_α and shear T_α forces (Lee and Foster, 2007). This condition is expressed by:

$$\frac{N_\alpha}{N_u} + \frac{T_\alpha}{T_u} + \frac{M_\alpha}{M_u} \geq 1 \tag{13}$$

where N_u, T_u and M_u are the strength capacity when subjected to axial, shear or bending individual loading conditions. For reinforcements of circular cross-section, in both the inclined and horizontal segments:

$$N_u = \sigma_u A_\alpha, \quad T_u = \sigma_u A_\alpha/\sqrt{3}, \quad M_u = 4\,\sigma_u r_\alpha^3/3, \tag{14}$$

where σ_u is the tensile strength of the reinforcement (see Fig. 2a). On the other hand, if Eq. (13) is not satisfied, debonding occurs.

In addition to reinforcement rupture and debonding, the matrix spalling is a phenomenon in which failure of the matrix occurs due to the local curvature and stretching of the reinforcement at the matrix crack surface. The volume of the matrix wedge spalled off depends on the external load, reinforcement cross section and inclination angle, and the matrix properties. Spalling mechanism does not occur when the transverse force induced on the matrix is lower than a critical resistant value (Laranjeira et al., 2010). To quantify the average matrix spalled volume, a simplified failure criterion is herein proposed that takes into account the resisting mechanism provided by the matrix R_{sp} and the force acting at the connection between the horizontal and inclined segments. In particular, experiments in (Cailleux et al., 2005) showed that the crack surface due to the matrix spalling is usually perpendicular to the inclined portion of the reinforcement, which implies that the main component of the spalling force is the shear force $T_i(L_i)$ at the end of the inclined segment. The distance at which the matrix wedge stabilizes depends on the length L_h of the horizontal portion of the reinforcement (see Fig. 1a). The resisting mechanism provided by the matrix R_{sp} is based on the assumption that the tensile strength of the matrix f_{ct} is the major parameter controlling the resistance against spalling. Therefore, if the transverse force $T_i(L_i)$ is higher than the resistant force R_{sp}, the spalling of the wedge occurs (as sketched in Fig. 1c). The evaluation of R_{sp} is carried out by:

$$T_i(L_i) > R_{sp} \quad \text{with} \quad R_{sp} = (A_1 + A_2) f_{ct}, \tag{15}$$

in which A_1 and A_2 are the lateral and front areas of the spalling volume indicated in Fig. 1b, that are related to the other geometric parameters of the model by:

$$\begin{aligned} A_1 &= L_h (L_h \tan(\varphi) + d), \\ A_2 &= L_h^2 \tan(\varphi) \sqrt{2}\,, \end{aligned} \tag{16}$$

where the angle φ represents the inclination of the fracture surfaces of the spalled concrete volume, which is assumed to be orthogonal to the inclined part of the reinforcement, i.e., $\varphi = \pi/2 - \theta$; on the other hand, the angle determining the area A_2 in Fig. 1b is taken to be 45^o, which is an acceptable value for the internal frictional angle of fracture in cement based materials (Laranjeira et al., 2010).

At each loading condition, the force corresponding to each possible failure mechanism is evaluated, and the lowest one determines the governing failure mode. It is noted that with the geometric and material parameters in Tabs. 1-2, the spalling of the matrix is always coupled with debonding or rupture of the

Table 1: Geometry parameters for modelling the smooth fibres (without the hook end).

Specimen	L_h	L_i	θ	$A_h = A_i$	$p_h = p_i$
C-aθ-Lt20	1 mm	19 mm	0^o, 30^o, 60^o	0.56 mm^2	2.35 mm
S-aθ-Lt30	1 mm	29 mm	0^o, 30^o, 60^o	0.56 mm^2	2.35 mm
L-aθ-Lt10	1 mm	9 mm	0^o, 30^o, 60^o	0.19 mm^2	1.57 mm

Table 2: Material parameters for the fibre-reinforced concrete considered.

Specimen	E [GPa]	σ_u [MPa]	τ_m [MPa]	τ_r [MPa]	u_I* [mm]	u_{II} [mm]	K [GPa]	K_α [kN]	v_I [mm]	v_{II} [mm]
C	200	1200	2.15	0.90	$0.20\,\exp(1.5\,\theta)$	$1.3\,u_I$	20	4.5	0.17	0.25
L	200	900	1.75	0.75	$0.17\,\exp(1.4\,\theta)$	$1.2\,u_I$	13	6.1	0.13	0.20

* The value of the inclination angle θ is expressed in radians.

reinforcement and takes place before the total fibre debonding or reinforcement rupture occur. Indeed, this coupling was experimentally observed in (Cunha et al., 2009; Robins et al., 2002).

3. Model implementation and validation

Due to nonlinear behaviour of materials and interaction between the mechanisms developed during reinforcement pull-out, the load-displacement relationship of a pull-out test was numerically obtained by solving the differential equations (6) with the constitutive laws for the fibre-matrix interface and matrix supporting foundation to the fibre (Eqs. (7) and (8)), applying an increasing displacement at the fibre exit point. The model has been implemented in Matlab employing the built-in routine `bvp4c` that solves nonlinear boundary value problems using an adaptive collocation method. One hundred points were considered in the discretization of each segment, being the points concentrated on the boundaries where relatively high gradient values for the variables are expected to occur. To improve the convergence of the method, at each increment of the applied displacement, the solution at the previous iteration was used as an initial guess. Therefore, the solution was obtained by using at least 250 increments of the applied displacement; at each increment the number of iterations necessary to achieve the convergence of the numerical algorithm was automatically controlled by the matlab `bvp4c` routine, according to the desired value of the tolerance, which was set to 10^{-4}.

At each increment, the values of the the axial N_α and shear T_α force, and the bending moment M_α are calculated from the solution, i.e., $N_\alpha = EA_\alpha u'_\alpha$, $T_\alpha = K_\alpha(\vartheta_\alpha - v'_\alpha)$ and $M_\alpha = EI_\alpha \vartheta'_\alpha$, and are compared to Eqs. (13) and (15) to assess the possible occurrence of fibre rupture or matrix spalling. When Eq. (15) is verified, the embedment length is changed by making the horizontal part of the reinforcement unbonded (Fig. 1c); this condition is implemented by letting to zero the support reaction q in Eq. (6.3) for the horizontal part. The simulation is stopped when one of the following conditions occur: (i) Eq. (13) is verified, meaning that the reinforcement has failed, (ii) the entire interface is in softening (region III in Fig. 2b) meaning that the debonding of the reinforcement has occurred.

To obtain a better insight into the pull-out mechanism of the system, numerical analyses have been performed using the finite-element program Abaqus, where a 2D plane stress model was implemented (Fig. 4). The thickness of the concrete block and of the reinforcement is assumed to be 0.60 mm, whereas the horizontal segment is 1 mm long; for the analysis two inclination angles, 30^o and 60^o, are considered. **A total number of 14.700 4-nodes elements with reduced integration (CPS4R) are used in the simulations with a finer mesh in the location where relatively high stress or strain gradients are expected to occur. The number of elements was set to guarantee mesh objectivity, which was assessed by running multiple simulations with an increased number of elements until the changes in results were negligible.** The support and loading conditions were simulated according to the characteristics of the commonly used test setup, and are shown in the same figure. The Concrete Damaged Plasticity (CDP) model was adopted to simulate the concrete nonlinear behaviour. In the CDP model, the theory of linear isotropic elasticity in combination with isotropic tensile and compressive plasticity are used to simulate the inelastic behaviour of concrete. The CDP model considers two main damage mechanisms: crack formation and

Table 3: Constitutive parameters used in the numerical simulation with Abaqus.

Concrete	f_{cc} (MPa)	E_c (GPa)	f_{ct} (MPa)	G_c (N/mm)		
	45	34.5	2.1	0.1		
CDP	w (deg)	e	f_{b0}/f_{c0}	$K_{c,surf}$	V	
	38	0.1	1.16	0.67	0	
Cohesive Interface	$\sigma_{n,max}$ (MPa)	$G_{n,b}$ (N/mm)	δ_n^{max} (mm)	$\sigma_{s,max}$ (MPa)	$G_{s,b}$ (N/mm)	δ_s^{max} (mm)
	2.1	0.1	0.21	2.7	1.8	0.27

propagation in tension; and elastoplasticity in compression. The constitutive parameters of the CDP model (dilation angle w, plastic potential eccentricity e, stress ratio f_{b0}/f_{c0} (ratio between the compressive strength in bi- and uni-compression stress field, f_{b0} and f_{c0}, respectively), shape of the loading surface $K_{c,surf}$, and viscosity parameter V) were estimated based on the recommended range of values by Abaqus manual and showed in Tab. 3.

The contact between reinforcement and concrete was modelled by a cohesive interface law with a linear softening response and the steel reinforcement has a linear behaviour until the rupture. The axial tensile strength ($\sigma_{n,max}$), the displacement at the maximum stress (δ_n^{max}), and the tensile fracture energy ($G_{n,b}$) of the interface were obtained from the tensile strength and fracture energy of the concrete, while the shear strength ($\sigma_{s,max}$), the displacement (δ_s^{max}) and the shear fracture energy ($G_{s,b}$) were obtained from Cunha et al. (2009). The values of the parameters for the constitutive law of the interface finite elements are presented in Tab. 3, whilst in Tab. 2 the values of the constitute laws of the developed analytical model are listed. For the steel reinforcement the same elastic modulus used in analytical model with a Poisson ratio of 0.3 was considered. **The values of the constitutive parameters were extracted from Cunha (2010), where extensive numerical simulations were carried out.**

The horizontal and transverse displacement fields obtained from the Abaqus and the developed analytical model are compared in Fig. 5, where a reasonable match is verified, with a larger discrepancy in the transition zone, due to the geometric difference between the two models. Indeed, to avoid the numerical

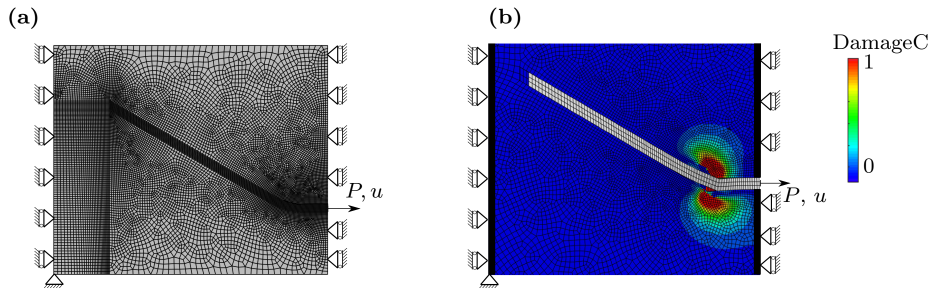

Figure 4: (a) Details of the finite element mesh adopted in the simulation for an angle of the reinforcement of 30 °, and (b) results of the simulations showing compression damage of the concrete matrix starting at the transition zone.

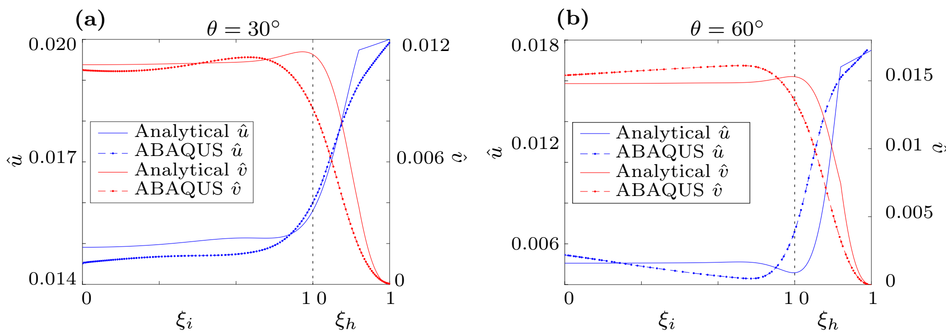

Figure 5: Vertical and horizontal dimensionless displacements for $\theta = 30^o$ (a) and $\theta = 60^o$ (b) for the proposed model and the corresponding Abaqus simulations.

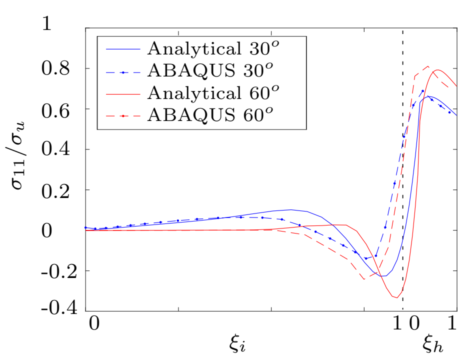

Figure 6: Variation of the normalised axial stress along the fibre for the proposed model and the Abaqus simulations.

issues related to possible stress concentration at the transition between the horizontal and inclined segments, a smoother transition between the two parts was implemented with a radius of curvature of 5 mm as seen in Fig. 4a. Figure 6 shows the normalised axial stress (σ_{11}) variation calculated from the proposed model and from the FE simulations by integrating the axial stress component over the typical cross section. It is noted that the average axial stress is accurately described, despite a part of the reinforcement being in compression due to the contact with the concrete in the transition zone. In addition, the degradation mechanism observed in the FE simulations is similar to the one predicted by the model. For the 30^o specimen, the first failure mechanism observed is the debonding of the interface that starts from the fibre exit point and moves towards the inclined segment; on the contrary, for the 60^o specimen, the degradation of the matrix occurs first, starting from the transition zone due to the concrete crushing seen in Fig. 4b. The same failure mechanisms are observed in the analytical model and will be discussed in details in the next section where the model is compared to experimental data.

4. Comparison to experiments

To evaluate the reliability of the proposed approach, slip vs pull-out force relationships are compared with those experimentally obtained by Cunha et al. (2009) and Leung and Shapiro (1999). The specimens adopted by Cunha et al. (2009) consisted of cylindrical concrete specimens with a single smooth steel fibre. The smooth steel fibres without a hook end in the embedded part, with diameter 0.75 mm and lengths $L_b = \{20.0, 30.0\}$ mm, were inserted under different inclination angles (0, 30 and 60 degrees) on a self-compacting concrete of 83.4 MPa mean compressive strength. **On the other hand, Leung and Shapiro (1999) performed pull-out tests on smooth fibres with $L_b = 10$ mm at different inclination angles (0, 30 and 60 degrees) on standard concrete with 36.5 MPa mean compressive strength.**

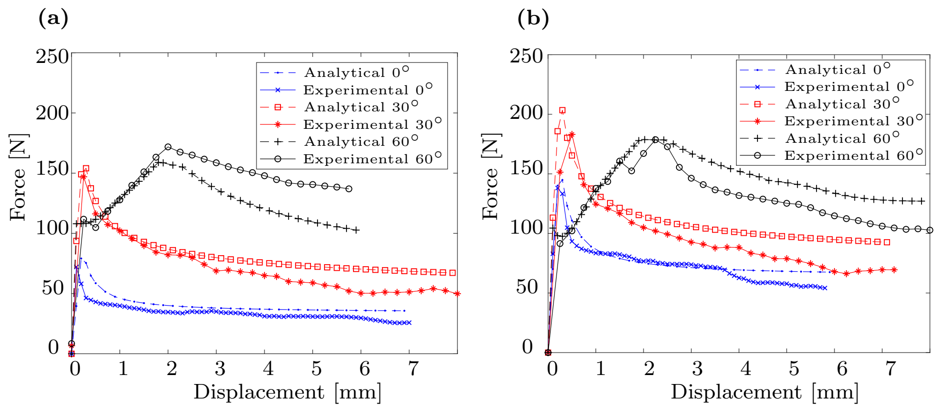

Figure 7: Force vs. displacement obtained experimentally and with the developed model for steel smooth fibres inclined at $L_b = 20$ mm (a) and $L_b = 30$ mm (b) (data from (Cunha et al., 2009)).

To simulate these fibres with the embedment part presenting certain inclination towards the normal to the crack plane (θ), a very small horizontal length L_h was chosen (1 mm in this case). Table 1 gives an overview of the geometric parameters of the steel fibres for both experiments and the constitutive paramaters are reported in Tab. 2, where the specimen C refer to the data in (Cunha et al., 2009), and L to the data in (Leung and Shapiro, 1999).

The values of the constitutive parameters were obtained by fitting the experimental data except for the Young modulus of the fibre and its ultimate strength, which were obtained from the literature. Due to the nonlinearity of the model, a multi-step optimization strategy was used. First, the values of the model simulating the interface were extracted from the experiments with the fibre at 0°, for which the properties involved in matrix spalling have a marginal influence. Then the concrete characteristics were found using the $\theta = 30°$ and $\theta = 60°$ data, since in these cases the stiffness and strength of the matrix are mobilized. The optimal values of the constitutive parameters were found at each step by carrying out a nonlinear minimization problem in Matlab with an objective function that weighed the data for $L_b = 30$ mm only; remarkably, the fitting for $L_b = 20$ mm is extrapolated from these values.

The results of the fitting are shown in Fig. 7, whereas the details of the different stages of the loading process as predicted by the analytical model are reported in Figs. 10-11. By analysing the results in Fig. 7, it is seen that the fibre inclination has a significant impact on the displacement at peak load, that increases as the inclination increases, mainly when matrix spalling occurs at fibre exit point. In addition, the peak pull-out load increases with the fibre embedment length. However by increasing both the embedment length and inclination of the fibre, the peak pull-out force tends to decrease since the occurrence of matrix spalling is being promoted. This effect is more pronounced for longer embedment lengths (Fig. 7b) and is due to higher portions of concrete being damaged and expelled off at the crack plane. When the spalling occurs, the horizontal part of the fibre can deform without any significant constraints, and the fibre effective embedment length decreases, thus the total force is reduced. To catch this behaviour, the parameter u_I of the bond-displacement constitutive law was made dependent on the angle θ as indicated in Tab. 2 (θ in radians). Therefore, the stiffness of the first branch of the bond interface law decreases with the increase of θ in order to indirectly simulate these complex micro-mechanisms at the fibre exit zone with a relatively simple strategy from the modelling perspective. Using this strategy, the proposed model could predict the different pull-out behaviour for the different orientations and different embedment lengths.

Figure 7 demonstrates that for inclination angles of 0 and 30^o, the nonlinear part of the ascending branch has a relatively small amplitude, starting almost at the peak force. After the maximum force is attained a sudden drop is observed, which corresponds to an abrupt increase of damage at the fibre-matrix interface. In the other hand, the concrete cracking and spalling for $60°$ fibre orientation have changed the pre-preak stage to an approximate bilinear configuration. In fact, after micro-spalling initiation the stiffness of the fibre pull-out process decreases, and some drops of fibre pull-out force with abrupt increase of fibre displacement occur due to matrix spalling propagation. Such dissimilar trends

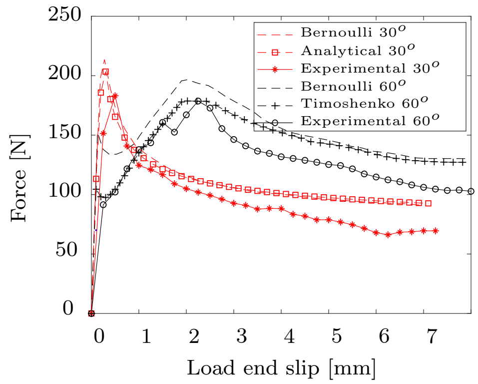

Figure 8: Comparative study between the Timoshenko beam model (Eq. (4)) and the Euler-Bernoulli beam model, which does not account for the shear deformability of the fibre (data from (Cunha et al., 2009) with $L_b = 30$ mm).

derive mainly from the different magnitudes of the transverse force, which occur at fibre exit point. The increase in the inclination angle increments the pressure imposed by the fibre on the surrounding matrix; since cementitious matrices are brittle in nature, whenever this pressure exceed a certain critical value, local failure tends to occur. **Whenever this phenomenon happens, small pieces of matrix spall-off, and a load drop can be observed on the pull-out curve. This load drop leads to a significant loss of stiffness that is well represented by the proposed model and is mainly due to the consideration of the shear deformability of the fibre. This is, in fact, confirmed by the results in Fig. 8 where both Timoshenko and Euler-Bernoulli models are compared against the data for the $30°$ and $60°$ specimen in Fig. 7b; the Euler-Bernoulli model, indeed, which does not account for the shear deformability of the fibre, overestimates the force at which the microspalling of the matrix starts developing and, as a result, cannot predict equally well the load-drop seen in the experiments.**

The fitting of the experiments by Leung and Shapiro (1999) is shown in Fig. 9. Three fibre inclination angles (θ = 0, 30 and 60 degrees) were tested by the authors and the results show that the model closely fit this behaviour. A close match of the peak force as

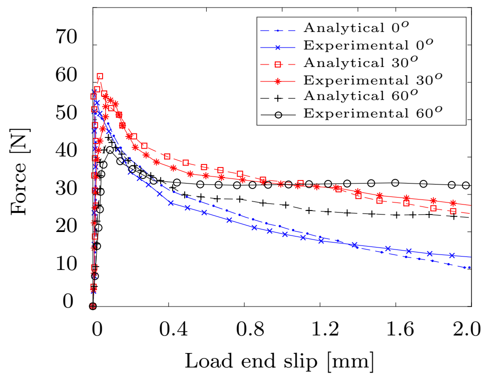

Figure 9: Force vs. displacement obtained experimentally from Leung and Shapiro (1999) and the developed model for steel smooth fibres with $L_b = 10$ mm.

well as of the corresponding displacement is achieved for the three angles. The increase of the displacement at peak force for higher angles, is most presumably due to the occurrence of microspalling, and is well-captured by the proposed model.

Finally, the different stages of the pull-out process as predicted by the model for 30^o and 60^o specimen are shown in Figs. 10 and 11. The delamination of the interface always started from the loaded end of the fibre and moves towards the inclined segment, as already seen in Alessi et al. (2016). The matrix behaviour is, however, different: the degradation begins at the transition zone and extends with the increase of the applied displacement. It should be noticed that the crushing propagation depends on the segment length, meaning that, when L_i is larger than L_h, a higher crushing propagation occurs in the inclined segment. Higher inclination angles cause the concrete crushing to start before the delamination of the interface (see Fig. 11 points B and C); in addition, the higher stress concentration in the matrix in the transition zone produces a higher crushing propagation, which in turn causes the pull-out force to start decreasing (point F in Fig. 11).

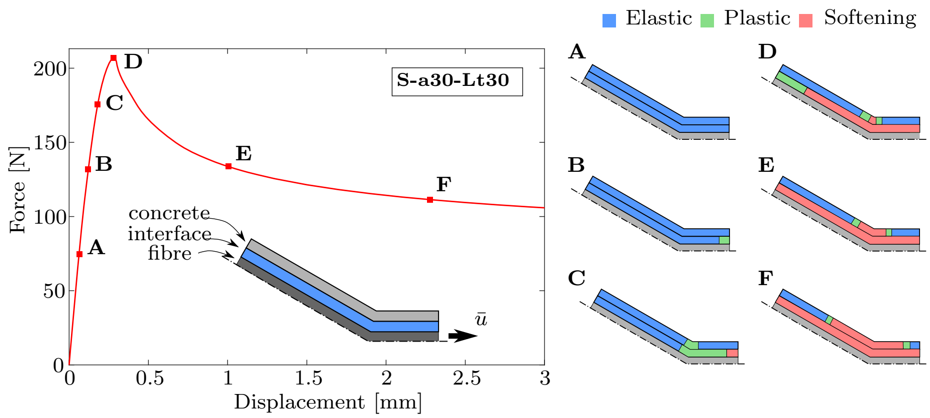

Figure 10: Different stages of the pull-out process for a 30^o fibre. The colours show the different regions in the material response (Elastic, Plastic, Softening). Due to symmetry only half of the geometry is shown.

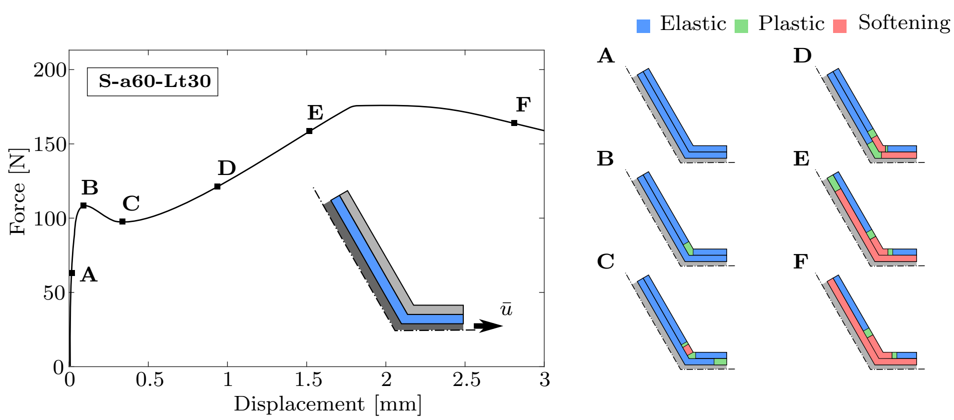

Figure 11: Different stages of the pull-out process for a 60^o fibre. The colours show the different regions in the material response (Elastic, Plastic, Softening). Due to symmetry only half of the geometry is shown.

5. Sensitivity Analysis

In order to optimize the material and geometric parameters of the system, a sensitivity analysis is carried out in this section. The constitutive parameters of the model are: E, K, K_h, K_i, σ_u, τ_m, τ_r, u_I, u_{II}, v_I, v_{II}; whereas the geometric parameters are L_h, L_i, θ, A_h, A_i, p_h and p_i. Therefore, the problem consists of 18 variables, but not all of them are independent as inferred from the normalised governing equations (Eqs. (6)). After demonstrating the reliability of the model in predicting the force vs displacement curves for smooth steel fibres, the model can be used to assess the influence of the model parameters on the fibre pull-out performance. In this context, the applicability of the model can even be extended for optimizing the geometry and material characteristics (mainly the tensile strength) of the fibre regarding the strength properties of the cement based medium. To that end, the dimensional analysis proposed here could be a powerful tool to undertake such a complex task.

First, the material choices were restricted to the values given in Tab. 2. Among the geometric parameters, the focus was placed on the embedment length $L_b = L_h + L_i$ and on the inclination angle θ, since preliminary studies have shown that these parameters have the largest impact on the peak force, dissipated energy and failure modes. The energy was obtained by calculating the area under the pull-out force versus displacement relationship. The peak force was normalised by the tensile strength of the fibre $P_u = \sigma_u A_h$, whilst the energy U with respect to the dissipated energy of an aligned fibre, U_0.

Experimentally, the influence of the embedment length and the inclination angle (θ) was assessed in Cunha et al. (2009). In order to avoid numerical issues, the value of L_h was kept fixed and equal to 1 mm as in the simulations of the previous sections. Figure 12a shows that the maximum peak force increase with the embedment length at each respective fibre orientation, as long as fibre rupture is not the governing failure mechanism. For embedment length smaller than $L_b = 50$ mm, the pull-out force tends to increase until a peak at 30^o, although for higher orientations, tensile rupture of the fibre is more likely to occur, with the fracture load appearing to decrease as fibre orientation increases. For higher orientation, in fact, the additional shear stresses and bending moment imposed on inclined segment leads to a reduction in the ultimate strength of the fibres, resulting in a smaller fracture load as confirmed by the experiments in (Laranjeira et al., 2010). Moreover, it is noticed that at higher inclination angles, the peak force reaches a maximum at lower embedment length and then remains almost constant, meaning that in FRC where fibres have a tendency to cross the cracks with a relatively high angle, and consequently to develop concrete spalling at the exit point of the fibre, no benefits in terms of fibre reinforcement are obtained by using longer fibres. Using smaller fibres but maintaining the fibre content unchanged, can, in these circumstances, provide higher reinforcement efficiency.

Figure 12b shows that the energy dissipated increases with θ and L_b, as long as the fibre do not fail by tensile rupture. The relationship between maximum energy and failure mode is clear. The energy is maximum at this debonding-fibre tensile rupture limit (Fig. 12b and 13). When the failure mode change from fibre debonding to fibre tensile rupture, a sharp decrease in energy occurs, then start to increase again for higher angles due to the increased friction in the pull-out process. Figure 13 shows the map of the failure modes for the different configuration in terms of θ and L_b. In smooth steel fibres, the relevant resisting mechanisms are the curvature at the fibre exit point and the consequent resistance offered by the surrounding matrix to the transversal pressure introduced by the fibre during its pull-out process; however, when the embedment length is less than 40 mm, they are not sufficient for the fibre to reach its full load capacity, since debonding of the fibre occurs as available experimental data demonstrate (Cunha et al., 2009; Fantilli and Vallini, 2007; Laranjeira et al., 2010; Zhan and Meschke, 2014). In the analyses carried out, the transition of failure mode from fibre debonding to fibre tensile rupture starts for an embedment length higher than $L_b = 40$ mm and higher orientations. Given that fibre rupture is an undesirable failure, due to the low dissipated energy, the pull-out model can then be used to provide some valuable insights and optimize the fibre

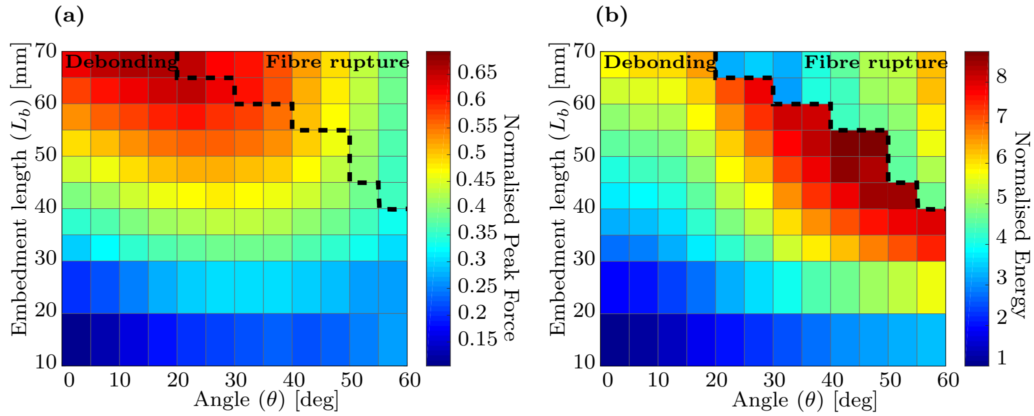

Figure 12: Contour plot of the peak force (a) and dissipated energy (b) for $\theta \in [0, 60]$ and $L_b \in [10, 70]$ mm. The thick dashed lines show the transition between two failure modes: complete debonding of the fibre from the matrix or fibre rupture.

characteristics for FRC.

Finally, the effects of fibre tensile strength (σ_u) and concrete compressive strength are investigated in Figs. 14 and 15. The analysis is carried out for two inclinations of the fibres, 30^o and 60^o degrees, with a bond length $L_b = 30$ mm and by keeping $L_h = 1$ mm. All the constitutive parameters are kept fixed as in Tab. 2, except for σ_u and K. The latter was made dependent on the concrete compressive strength f_{cm} as suggested by Zhan and Meschke (2014), through the relationship $K = a\sqrt{f_{cm}}$, where the coefficient a was determined by fitting the experimental data in (Cunha et al., 2009), for which the foundation modulus was $K = 20$ GPa and the mean compressive strength of the concrete was 83.4 MPa. The range of the tensile strengths of the fibres and compressive strength of the concrete were set considering that commonly available steel fibres have a tensile strength between 500 MPa up to 2500 MPa, whereas in the technology of FRC, different concrete mixtures with compressive strength ranging from 25 MPa up to 200 MPa are used.

The results show that the concrete strength and the fibre tensile strength have a significant impact on both peak force and energy dissipation, with a significant increase when the compressive strength of the concrete is increased.

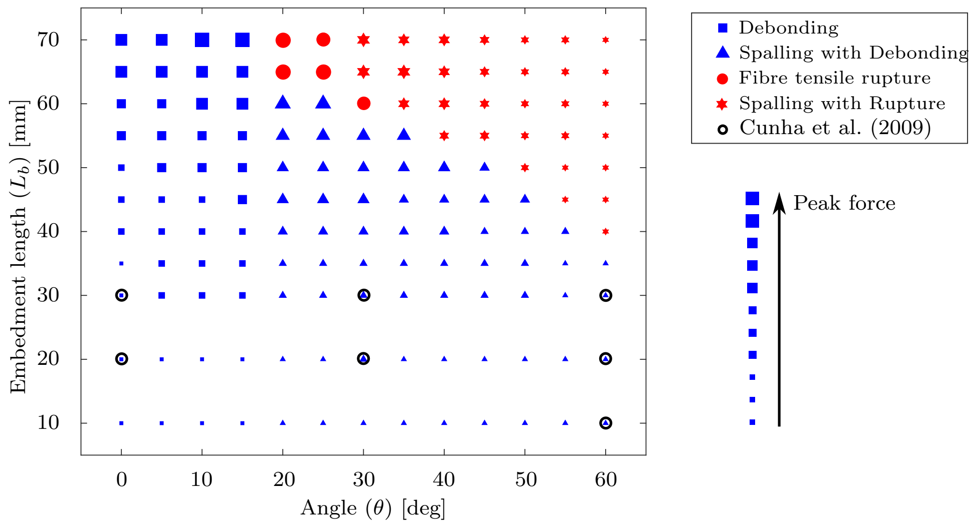

Figure 13: Failure mode map in the θ and L_b space for the SFRC used in (Cunha et al., 2009).

When fibre debonding is the main failure mode of the FRC, an increase in the fibre tensile strength does not have any significant impact neither on the peak force nor on the energy dissipation, since the full capacity of the fibre is not reached. The peak force for the 60° specimen (Fig. 14b) is a lower than the 30° specimen even for higher concrete and fibre strength, due to the stress concentration at the transition zone that causes the premature failure of the fibre or the spalling of the matrix. In contrast, the matrix spalling produces an increase in the dissipated energy as seen in Fig. 15b, mainly due to the attainment of the peak force at higher displacement values compared to a 30° specimen. As a design guideline, the analysis suggests that the use of high strength concrete has the potential to increase both peak force and energy dissipation by 80%.

6. Conclusions

In this paper, the pull-out behaviour of reinforcements with a finite embedment length in cracked cement based materials has been investigated by means of a novel analytical model that has required a computational strategies for deal-

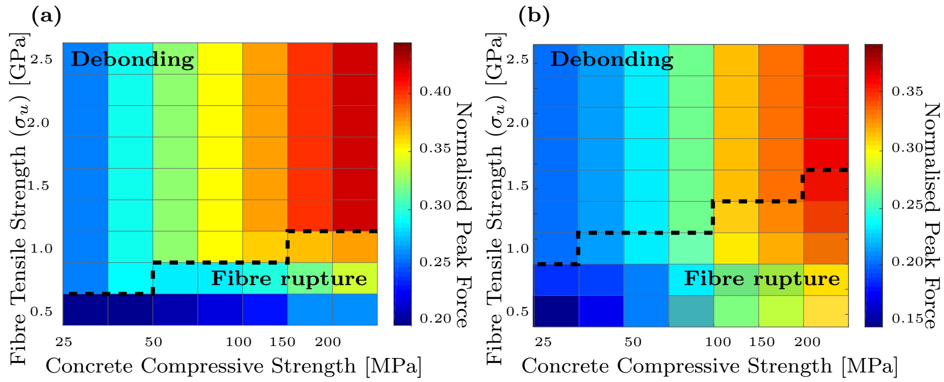

Figure 14: Contour plot of the normalised peak force for 30^o (a) and 60^o (b) fibres, for a concrete strength in the rage $[25, 200]$ MPa and fibre tensile strength in $[500, 2500]$ MPa. The normalisation is carried out for a fibre with $P_u = \sigma_u A_h$ given in Tab. 2.

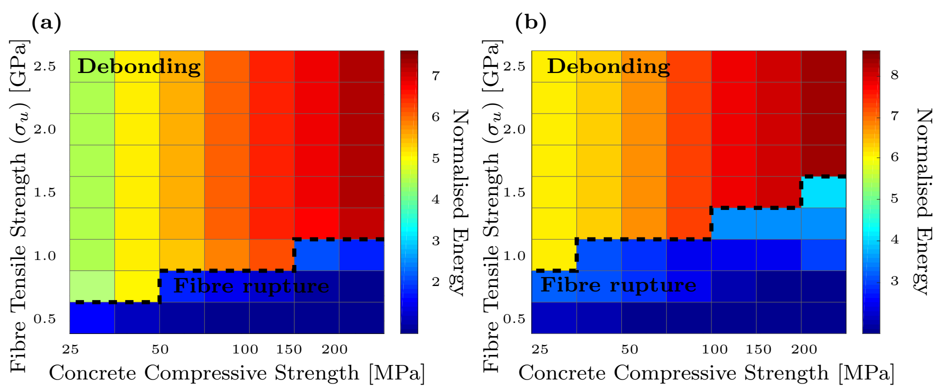

Figure 15: Contour plot of the normalised energy for 30^o (a) and 60^o (b) fibres for a concrete strength in the rage $[25, 200]$ MPa and fibre tensile strength in $[500, 2500]$ MPa. The normalisation is carried out with respect to a 0° fibre with the material parameters in Tab. 2 as in Fig. 12. The thick dashed lines show the transition between two failure modes: complete debonding of the fibre from the matrix or fibre tensile rupture.

ing with the involved nonlinear complex mechanism. The reinforcement-matrix system is modelled as a Timoshenko beam resting on a nonlinear foundation. A cohesive-like relationship is used to describe both the sliding at the fibre-matrix interface and the stiffness provided by the surrounding matrix to the transversal movement of the fibre towards the matrix. These constitutive laws are composed by an elastic, plastic and softening stages in order to have sufficient flexibility for simulating the different damage level that occur during the activation of these mechanisms in the fibre pull-out. **These features confer to the model two main characteristics: (i) it can account for the effects the reinforcement geometry, strength, embedded length and inclination angle; (ii) it is able to simulate the bending of the inclined fibre, the damage of the concrete matrix at the fibre exit point, and the change on the embedment length due to matrix spalling. These features were mostly neglected by previous literature contributions.**

Both finite element simulations and a comprehensive comparison of experimental data available in the assessed literature have highlighted the good predicting capabilities of the model, that was able to accurately match the peak force and the energy dissipated during the pull-out process. By carrying out a parametric analysis, it was shown that the pull-out response of fibre reinforced concrete is predominantly influenced by the embedment length, angle and failure modes. In particular, the results highlight that:

- **fibre rupture starts with embedment lengths greater than** 40 **mm and higher inclination angles. In some applications, this is an undesirable failure mode as it implies a low dissipated energy;**
- **fibres oriented at 30^o with embedment lengths of** 40 **mm have a peak pull-out force** 25 **% higher than the zero degree fibres and, at the same time, dissipates** 50 **% more energy during the pull-out process;**
- **when the material properties are tuned to have the debonding**

of the fibre as the main failure mode of the FRC, the sensitivity analysis showed that the use of a high-strength concrete has the potential to increase both peak force and energy dissipation by 80 **%.**

These results show that the combination of the parametric analysis and the versatility of the proposed model, constitute an invaluable tool to optimize the design of fibre reinforced concrete, but is suitable to be used also for other type or reinforcement. Future research work will require the application of the proposed model to more complex fibres geometry such as the ones of hooked end fibres. This can be achieved by replicating the proposed model in multiple branches with the proper boundary conditions between each branch.

Acknowledgements

J.A.O. Barros wishes to acknowledge the support by FEDER through the Operational Program for Competitiveness Factors – COMPETE and from the Portuguese Foundation for Science and Technology (FCT) under the project FCOMP-01-0124-FEDER-014844.

References

C. E. Bakis, L. C. Bank, V. L. Brown, E. Cosenza, J. F. Davalos, J. J. Lesko, a. Machida, S. H. Rizkalla, T. C. Triantafillou, Fiber-reinforced polymer composites for construction - State-of-the-art review, Journal of Composites for Construction 6 (2) (2002) 73–87.

A. Meda, F. Minelli, G. Plizzari, P. Riva, Shear behaviour of steel fibre reinforced concrete beams, Materials and structures 38 (3) (2005) 343–351.

J. A. O. Barros, S. J. Foster, An integrated approach for predicting the shear capacity of fibre reinforced concrete beams, Engineering Structures Journal 174 (2018) 346–357, doi:10.1016/j.engstruct.2018.07.071.

J. A. O. Barros, J. A. Figueiras, Experimental behaviour of fibre concrete slabs on soil, Mechanics of Cohesive-frictional Materials: An International Journal on Experiments, Modelling and Computation of Materials and Structures 3 (3) (1998) 277–290.

J. A. O. Barros, M. Rezazadeh, J. P. Laranjeira, M. R. Hosseini, M. Mastali, H. Ramezansefat, Simultaneous flexural and punching strengthening of RC slabs according to a new hybrid technique using U-shape CFRP laminates, Composite Structures 159 (2017) 600–614.

N. Ganesan, J. R. Murthy, Strength and behavior of confined steel fiber reinforced concrete columns, Materials Journal 87 (3) (1990) 221–227.

G. Tiberti, F. Minelli, G. Plizzari, Reinforcement optimization of fiber reinforced concrete linings for conventional tunnels, Composites Part B: Engineering 58 (2014) 199–207, doi:10.1016/j.compositesb.2013.10.012.

A. M. Brandt, Fibre reinforced cement-based (FRC) composites after over 40 years of development in building and civil engineering, Composite structures 86 (1-3) (2008) 3–9.

A. E. Naaman, H. Najm, Bond–Slip Mechanisms of Steel Fibers in Concrete, ACI Materials Journal 88 (1991) 135–145, doi:10.14359/1896.

A. Bentur, S. Mindess, Fibre Reinforced Cementitious Composites, Francis & Taylor, UK, 2007.

V. M. Cunha, J. A. O. Barros, J. M. Sena-Cruz, Pullout behavior of steel fibers in self-compacting concrete, Journal of Materials in Civil Engineering 22 (1) (2009) 1–9.

A. P. Fantilli, P. Vallini, A cohesive interface model for the pullout of inclined steel fibers in cementitious matrixes, Journal of Advanced Concrete Technology 5 (2) (2007) 247–258.

F. Isla, G. Ruano, B. Luccioni, Analysis of steel fibers pull-out. Experimental study, Construction and Building Materials 100 (2015) 183–193.

F. Laranjeira, C. Molins, A. Aguado, Predicting the pullout response of inclined hooked steel fibers, Cement and Concrete Research 40 (10) (2010) 1471–1487.

C. K. Y. Leung, N. Shapiro, Optimal steel fiber strength for reinforcement of cementitious materials, Journal of Materials in Civil Engineering 11 (2) (1999) 116–123.

H. Mazaheripour, J. A. O. Barros, J. M. Sena-Cruz, Tension-stiffening model for FRC reinforced by hybrid FRP and steel bars, Composites Part B: Engineering 88 (2016) 162–181.

P. Robins, S. Austin, P. Jones, Pull-out behaviour of hooked steel fibres, Materials and Structures 35 (7) (2002) 434–442.

Y. Zhan, G. Meschke, Analytical model for the pullout behavior of straight and hooked-end steel fibers, Journal of Engineering Mechanics 140 (12) (2014) 91–104.

E. Zīle, O. Zīle, Effect of the fiber geometry on the pullout response of mechanically deformed steel fibers, Cement and Concrete Research 44 (2013) 18–24.

A. Bilotta, F. Ceroni, J. A. O. Barros, I. Costa, A. Palmieri, Z. K. Szabó, E. Nigro, S. Matthys, G. L. Balazs, M. Pecce, Bond of NSM FRP-Strengthened Concrete: Round Robin Test Initiative, Journal of Composites for Construction 20 (1) (2016) 04015026.

A. Caggiano, E. Martinelli, C. Faella, A fully-analytical approach for modelling the response of FRP plates bonded to a brittle substrate, International Journal of Solids and Structures 49 (17) (2012) 2291–2300.

E. Cosenza, G. Manfredi, R. Realfonzo, Behavior and modeling of bond of FRP rebars to concrete, Journal of composites for construction 1 (2) (1997) 40–51.

J. M. Sena-Cruz, J. A. O. Barros, Modeling of bond between near-surface mounted CFRP laminate strips and concrete, Computers & Structures 82 (17) (2004) 1513–1521.

L. De Lorenzis, A. Rizzo, A. La Tegola, A modified pull-out test for bond of near-surface mounted FRP rods in concrete, Composites Part B: Engineering 33 (8) (2002) 589–603.

M. Echeverria, R. Perera, Three dimensional nonlinear model of beam tests for bond of near-surface mounted FRP rods in concrete, Composites Part B: Engineering 54 (2013) 112–124.

F. Focacci, A. Nanni, C. Fellow, E. Bakis, Local Bond-Slip Relationship for FRP Reinforcement in Concrete, J. Compos. Constr 4 (February) (2000) 24–31.

R. Seracino, N. M. Jones, M. Ali, M. W. Page, D. J. Oehlers, Bond strength of near-surface mounted FRP strip-to-concrete joints, Journal of Composites for Construction 11 (4) (2007) 401–409.

V. C. Li, Y. Wang, S. Backer, Effect of inclining angle, bundling and surface treatment on synthetic fibre pull-out from a cement matrix, Composites 21 (2) (1990) 132–140.

G. G. Lee, S. J. Foster, Behaviour of steel fibre reinforced mortar in shear II: Gamma ray imaging, UNICIV Report R-445 UNSW, UNSW, Sydney, Australia, 2006.

G. G. Lee, S. J. Foster, Behaviour of steel fibre reinforced mortar in shear III: Variable engagement model II, UNICIV Report R-448 UNSW, UNSW, Sydney, Australia, 2007.

W. Kalupahana, Anchorage and bond behaviour of near surface mounted fibre reinforced polymer bars, Ph.D. thesis, University of Bath, 2009.

Y. Wang, L. Tham, Y. Cheung, Beams and plates on elastic foundations: a review, Progress in Structural Engineering and Materials 7 (4) (2005) 174–182.

Y. Wang, Mechanics of fiber reinforced cementitious composites, Ph.D. thesis, Massachusetts Institute of Technology, 1989.

S. Chasioti, Hybrid Steel Fibre Reinforced Concrete in Shear: From the Material to the Structural Level, Ph.D. thesis, University of Toronto, 2017.

T. S. Ng, S. J. Foster, M. L. Htet, T. N. S. Htut, Mixed mode fracture behaviour of steel fibre reinforced concrete, Materials and structures 47 (1-2) (2014) 67–76.

E. Cailleux, T. Cutard, G. Bernhart, Pullout of steel fibres from a refractory castable: experiment and modelling, Mechanics of Materials 37 (4) (2005) 427–445.

V. M. Cunha, Steel fibre reinforced self-compacting concrete (from micromechanics to composite behavior), Ph.D. thesis, Escola de Engenharia da Universidade do Minho, 2010.

R. Alessi, J. Ciambella, A. Paolone, Damage evolution and debonding in hybrid laminates with a cohesive interfacial law, Meccanica (2016) 1–13.